Hindawi Publishing Corporation
EURASIP Journal on Wireless Communications and Networking
Volume 2011, Article ID 362521, 12 pages
doi:10.1155/2011/362521

Research Article

An Analytical Modeling of Polarized Time-Variant On-Body Propagation Channels with Dynamic Body Scattering

Lingfeng Liu,[1,2] Farshad Keshmiri,[1] Christophe Craeye,[1] Philippe De Doncker,[2] and Claude Oestges[1]

[1] *ICTEAM Electrical Engineering, Université Catholique de Louvain, 3 Place du Levant, 1348 Louvain-la-Neuve, Belgium*
[2] *OPERA Department, Université Libre de Bruxelles, CP 194/5, Avenue F. D. Roosevelt 50, 1050 Bruxelles, Belgium*

Correspondence should be addressed to Lingfeng Liu, lingfeng.liu@uclouvain.be

Received 5 October 2010; Accepted 13 January 2011

Academic Editor: Dries Neirynck

On-body propagation is one of the dominant propagation mechanisms in wireless body area networks (WBANs). It is characterized by near-field body-coupling and strong body-scattering effects. The temporal and spatial properties of on-body channels are jointly affected by the antenna polarization, the body posture, and the body motion. Analysis on the time variant properties of on-body channels relies on a good understanding of the dynamic body scattering, which is highly dependent on specific scenarios. In this paper, we develop an analytical model to provide a canonical description of on-body channels in both time and space domains to investigate the on-body propagation over the trunk surface of a walking human. The scattering from the arms and the trunk in different dimensions is considered with a simplified geometrical description of the body and of the body movements during the walk. A general full-wave solution of a polarized point source with multiple cylinder scattering is derived and extended by considering time evolution. The model is finally validated by deterministic and statistical comparisons to different measurements in anechoic environments.

1. Introduction

Wireless body area networks (WBANs) are innovative short-range wireless networks enabling communication between compact devices, which are placed inside, on, or around the human body. The promising capability of WBANs to convey biomedical information and personal data has attracted a vast range of wireless body-centric applications in recent years [1].

Wireless medical applications, such as wireless monitoring and remote healthcare, are important applications of WBANs. These applications have strict requirements on the power consumption and communication reliability, which have to be supported by low-power, long-term communication technologies like ZigBee [2, 3]. In these technologies, biomedical signals, for example, electrocardiography (ECG) or blood pressure, are detected and transmitted from spatially distributed sensors to a body-worn data collector for processing and transmitting to the outside world. Such transmission relies on the signal waves propagating on the surface of the human body, that is, on-body propagation. Unlike conventional large-scale propagation (indoors, outdoors, etc.), on-body propagation usually occurs in the near-field and undergoes strong body-coupling and body-scattering effects. Although realistic on-body channels are also affected by scattering from the objects surrounding the body, the particularity of on-body scattering is that it is always present, and that its characteristics are largely independent of the off-body environment. Moreover, on-body scattering also significantly modifies antenna radiation patterns, further affecting the level of off-body versus on-body contributions [4, 5]. For these reasons, a separate study of on-body scattering is fundamental to understand WBAN propagation in both theoretical analysis and practical applications.

Body-scattering results from the joint scattering from different body components (trunk, arms, legs, etc.). Due to the finite size and complex shape of the body, the impact of body scattering significantly differ depending on the antenna locations on the body. This will lead to different on-body path loss in different regions and dimensions on the body. In the time domain, certain body motions also cause body scattering to become dynamic, which results in time-variant on-body channel fading. However, given the large variety of antenna positions and body motions, an effective characterization of the on-body channels should be scenario specific with well-defined spatial distributions of on-body channels and patterns of the body movements.

The importance of the polarization has also been addressed by most WBAN studies [6]. Yet, the investigations are not sufficient because of measurement limitations and analyzing difficulties. The polarization is another sensitive parameter that affects both the on-body path loss and fading. There are two basic types of polarizations: tangential and normal to the body surface. Propagations in different polarizations along different dimensions on the body are usually distinct. In practical applications, polarization of the antennas can easily be modified by the posture and movement of the body, which will introduce significant disturbance on the link quality and the performance of the on-body communications, as demonstrated in [6]. A specific and analytical investigation on the polarization is thereby necessary to better understand the mechanism of on-body propagation and to properly design on-body communication systems.

Studies on WBAN propagation resort to various approaches. Empirical investigations have been widely adopted as in [7–10]. This approach reflects the reality but is insufficient to get an insight on the physical mechanisms involved in on-body scattering. Complex Finite-Difference Time-Domain (FDTD) simulations as in [11, 12] is another popular method to describe on-body propagation with a high resolution, but it is also quite time consuming if the dynamic body scattering is simulated. Analytical modeling, as studied in [13–15] with simplified geometric descriptions of the human body, is a compromise between precision and efficiency to describe the essential properties of on-body channels in different domains. Analytical models are also able to provide canonical channel characterizations with sufficient details, for example, on the spatial correlation to exploit the channel spatial diversity for communication enhancing techniques like cooperative multilink [16].

In this work, we develop an analytical model with respect to a typical on-body propagation scenario on a walking human being. The investigated on-body transmissions are located on the trunk surface, where the scattering from the trunk and the arms are considered. Cylindrical shapes are introduced to describe the trunk and arms, while the body motion is modeled by simplified arm traces in the azimuth plane. An arbitrarily polarized point source is considered in the model and the general full-wave solution of the source with multiple cylinder scattering is derived and extended to include time evolution. The model is finally validated through deterministic and statistical comparisons with different on-body propagation measurements in anechoic environment.

The paper is organized as follows. Sections 2 and 3, respectively, describe the investigated on-body propagation scenario and the modeling approach. In Section 4, the field solution is derived, with its extension to time evolution. The experimental model validation is presented in Section 5, and conclusions of the current work are drawn in Section 6.

2. Scenario Description

We consider a specific scenario of a walking human with a natural posture as depicted in Figure 1(a). The typical body movements during the walk are composed of two parts, the footwork and the arm swing. Both of them are rhythmic and quasiperiodic processes. In this scenario, the transmitter (Tx) and the receiver (Rx) of an on-body channel are both located on the trunk surface, as marked in Figure 1(b). It is assumed that on-body transmissions on the trunk are less affected by the scattering from the legs, so that the dominant scattering effects are from trunk and arms. Both Tx and Rx are assumed to be small-sized sensors that are fixed on the trunk surface with invariant positions and constant distance to the skin.

3. Body and Current Source Modeling

In the described scenario, we use three infinite, homogeneous, and lossy cylinders to model the trunk and the arms as in Figure 2(a). Although the elliptic cylinder is closer to the actual shape of the trunk as studied in [15], the complexity to analytically solve the scattering from the elliptic cylinder will be dramatically high, yet the improvement brought to the model is limited. The cylinders are then vertically placed and are allowed to have parallel movements in the azimuth plane. The conductivity of the cylinders is determined by the cole-cole model [17], and the cylinders are assumed to be composed by dry skin. The permeability, permittivity, and wavenumber in free space and in the cylinders are denoted by (μ_0, ϵ_0, k_0) and (μ, ϵ, k), respectively.

The Tx antenna is modeled by a polarized point source with constant electric current intensity, I. The polarization of the source is described by a direction vector, as in Figure 2(b). In view of the regular geometry of the body, the source is fixed at height $z = 0$.

The sizes and positions of the cylinders and of the source in the azimuth plane are described in the global polar coordinate in Figure 2(c). For simplicity, the cylinder representing the trunk is located at the global origin. The scenario can be generalized as a number of P cylinders being vertically placed with a polarized point source located in the azimuth plane $z = 0$. The radii of different cylinders are denoted as r_p, p being the index of the cylinder. We attributed a local coordinate (ϕ_p, ρ_p) to each cylinder that the center of the cylinder is located at its local origin, denoted as O_p. The position of the source in azimuth is denoted as (ϕ_s, ρ_s) in the global coordinate system, and (ϕ_{ps}, ρ_{ps}) in each local coordinate system.

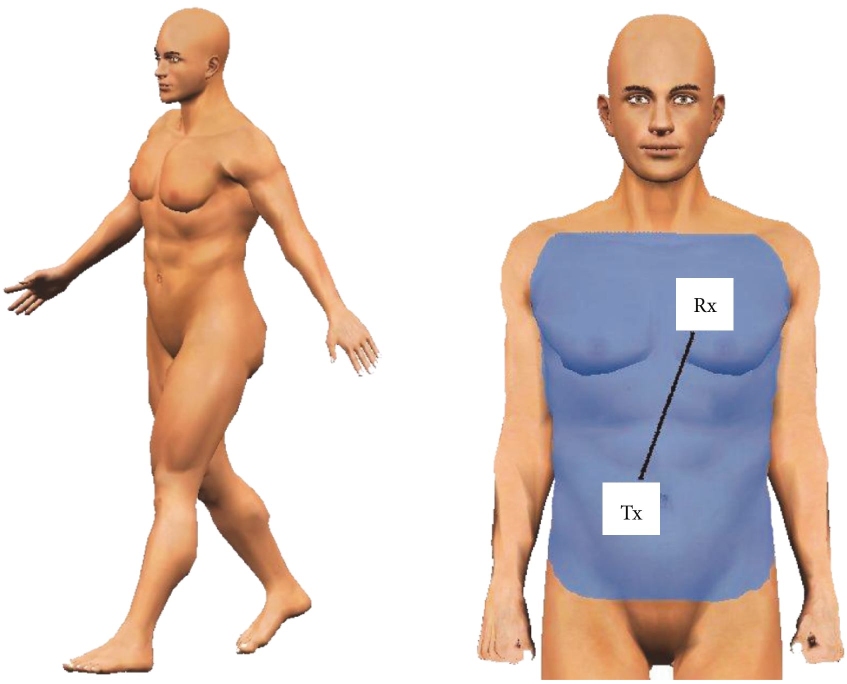

(a) Walking scenario with normal posture and movements

(b) Distribution of Tx and Rx. Both of them are located on the trunk surface

Figure 1: The investigated on-body propagation scenario on a walking human.

4. Field Solution

4.1. General Structure. The scattering problem in the model contains two parts: the representation of point source field and the full-wave solution of multiple cylinder scattering.

In [13], an integration method was introduced to represent a point current source by Fourier series of line current source, as expressed by

$$\mathbf{J} = \frac{I}{2\pi\rho_s}\delta(\rho - \rho_s)\int \sum_{m=-\infty}^{+\infty} e^{jm(\phi-\phi_s)}e^{-jk_z z}\mathbf{v}dk_z, \qquad (1)$$

where $k_z = \sqrt{k^2 - k_\rho^2}$ is the wavenumber along the z direction, k_ρ is the wavenumber along the ρ direction, and $\mathbf{v}$ is the direction vector of the source polarization. The sum of complex exponentials in (1) denotes the decomposition of the line source into cylindrical current sheets.

By (1), the point source scattering is equivalently expressed by the integration of line source scattering with different values of k_z, as

$$\begin{aligned}\mathbf{E}_{\text{point}}(\rho,\phi,z) &= \frac{1}{2\pi}\int_{-\infty}^{+\infty}\mathbf{E}_{\text{line}}\left(\rho,\phi,k_\rho\right)e^{-jk_z z}dk_z,\\ \mathbf{H}_{\text{point}}(\rho,\phi,z) &= \frac{1}{2\pi}\int_{-\infty}^{+\infty}\mathbf{H}_{\text{line}}\left(\rho,\phi,k_\rho\right)e^{-jk_z z}dk_z.\end{aligned} \qquad (2)$$

The contour of poles through proper integration path is also well described in [13].

The multiple cylinder scattering has been investigated by earlier studies as in [18, 19] for plane wave propagation. This paper will focus on the full-wave solution of a polarized line source with multiple-cylinder scattering. Conventionally, the total field is composed by the incident field from the line source and the scattered fields from the cylinders.

In (1), the line source inherits the polarization of the point source. The source current is then decomposed into polarization components along z, ϕ, and ρ directions, as in Figure 2(b). The current intensity of each polarization component fulfills $I = \sqrt{|I_\rho|^2 + |I_\phi|^2 + |I_z|^2}$. The total incident field is then the summation of the incident field from each polarization component. With the principles in [13, 20], the incident fields from each polarization component along z, ϕ, and ρ directions can be expressed, respectively, as the summation of cylindrical harmonics over different orders m, as

$$\begin{aligned}E_{m,\alpha}^{i} &= E_{m,\alpha}^{iz} + E_{m,\alpha}^{i\phi} + E_{m,\alpha}^{i\rho},\\ H_{m,\alpha}^{i} &= H_{m,\alpha}^{iz} + H_{m,\alpha}^{i\phi} + H_{m,\alpha}^{i\rho},\end{aligned} \qquad (3)$$

where, for example, $E_{m,\alpha}^{iz}$ and $H_{m,\alpha}^{iz}$, $\alpha = z/\phi/\rho$, denote the incident E and H fields from the z-polarization component along the α direction at order m. Equation (3) provides the complete incident field expression for arbitrary polarized current source along different dimensions.

In [13], the explicit numerical expression of the incident fields from polarization components I_z and I_ϕ were given. In this work, the numerical expression of the incident field from polarization component I_ρ is derived in Section 4.2.

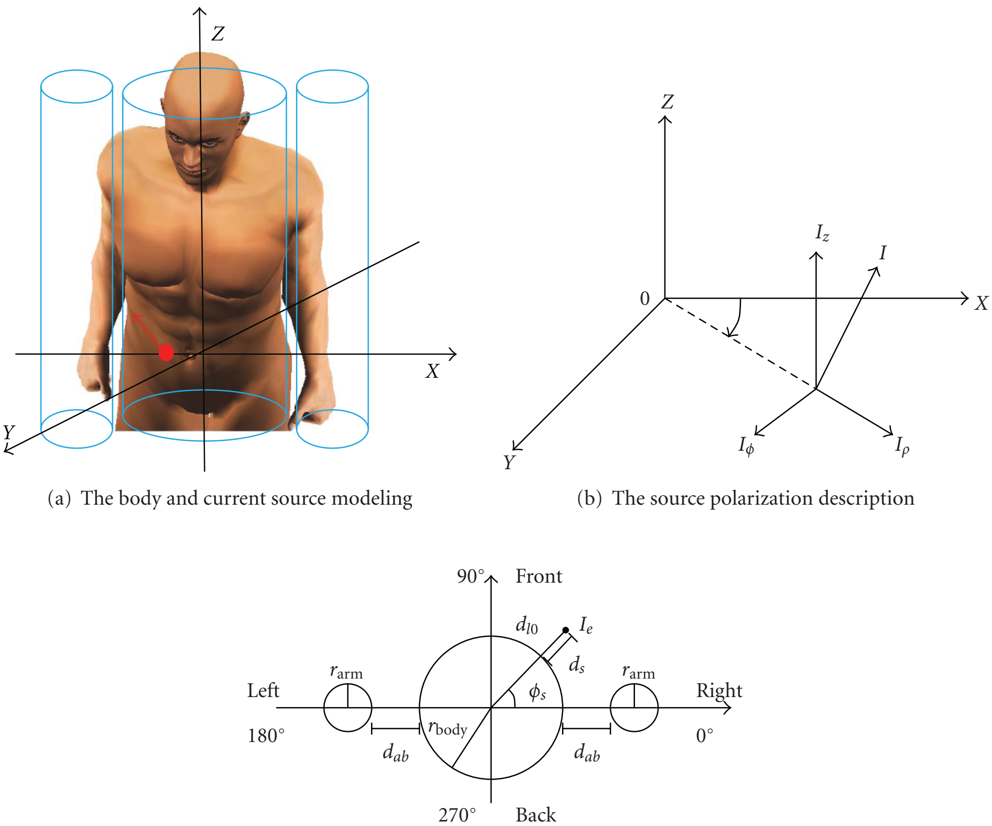

(a) The body and current source modeling

(b) The source polarization description

(c) Geometric quantization of the body and the source in azimuth plane. r_{body} is the trunk radius, r_{arm} is the arm radius, d_{ab} is the distance between the arm and the trunk, and d_s is the distance from the source to the trunk surface. The $d_{l0} = (r_{\text{body}}+d_s)\phi_s$ is the corresponding surface distance from the source to the trunk central

FIGURE 2: The human body and transmitter modeling by three lossy cylinders and one polarized point source.

The total scattered fields can be viewed as the summation of the individual scattered field from each cylinder. By [13], the individual scattered field can be expressed as the summation of cylindric harmonics in its local coordinate system. Normally, at order m, the scattered field from cylinder p along z direction can be expressed in its local coordinate as:

$$E^{s,p}_{m,z}\left(\rho_p,\phi_p\right) = \begin{cases} A^p_m J_m\left(k_\rho \rho_p\right) e^{jm(\phi_p-\phi_{ps})}, & \rho_p \le r_p, \\ B^p_m H^{(2)}_m\left(k_{\rho 0}\rho_p\right) e^{jm(\phi_p-\phi_{ps})}, & \rho_p > r_p, \end{cases}$$
$$H^{s,p}_{m,z}\left(\rho_p,\phi_p\right) = \begin{cases} C^p_m J_m\left(k_\rho \rho_p\right) e^{jm(\phi_p-\phi_{ps})}, & \rho_p \le r_p, \\ D^p_m H^{(2)}_m\left(k_{\rho 0}\rho_p\right) e^{jm(\phi_p-\phi_{ps})}, & \rho_p > r_p, \end{cases} \tag{4}$$

where J_m is the Bessel function of the first kind, and $H^{(2)}_m$ is the Hankel function of the second kind. The scattered field along the other directions ϕ and ρ can be directly derived via (4) by [20].

The scattered field parameters (A^p_m, B^p_m, C^p_m, D^p_m) can be solved by satisfying the following boundary conditions on each cylinder surface

$$E^{t,p}_{z1} = E^{t,p}_{z2}, \quad E^{t,p}_{\phi 1} = E^{t,p}_{\phi 2}, \quad \rho_p = r_p,$$
$$H^{t,p}_{z1} = H^{t,p}_{z2}, \quad H^{t,p}_{\phi 1} = H^{t,p}_{\phi 2}, \quad \rho_p = r_p, \tag{5}$$

where, for example, $E^{t,p}_{z1}$ and $E^{t,p}_{z2}$ represent the total E fields along the z direction just inside and outside the surface of cylinder p. The total fields outside cylinder p includes the incident field from the line source, which requires a local expression of the incident field from the line source as in (3) with its local polarization components I_z, I_{ρ_p}, and I_{ϕ_p}. In the presence of multiple cylinders, the total field outside cylinder p should also include the scattered fields from the other cylinders q, which are originally expressed in local coordinates q. With the above aspects considered, the boundary condition $E_{z1}^{t,p} = E_{z2}^{t,p}$ in (5) is further expanded as

$$\sum_{m=-\infty}^{+\infty} E_{m,z}^{s,p}\left(\rho_p,\phi_p\right) = \sum_{m=-\infty}^{+\infty} E_{m,z}^{i,p}\left(\rho_p,\phi_p\right) + \sum_{m=-\infty}^{+\infty} E_{m,z}^{s,p}\left(\rho_p,\phi_p\right) + \sum_{q\neq p}^{P}\sum_{n=-\infty}^{+\infty} E_{n,z}^{s,q}\left(\rho_q,\phi_q\right), \quad \rho_p = r_p, \tag{6}$$

where $E_{m,z}^{i,p}(\rho_p,\phi_p)$ is the local incident field at order m along z direction, and P is the total number of the cylinders. The same expansion should also be applied to the boundary condition $H_{z1}^{t,p} = H_{z2}^{t,p}$, and the remaining two boundary conditions in (6) can be derived through the principles in [20]. This forms the basic structure of the multiple cylinder scattering.

4.2. Incident Field of Line Source with Normal Polarization. A line source in Figure 2(c) with tangential polarization can be decomposed into cylindrical current sheets [13]. For normal polarization $\mathbf{J} = I_\rho\hat{\rho}$, a modified addition theorem for Bessel functions should be used to produce a cylindrical wave decomposition of the incident field [21, 22].

The vector potential, $\mathbf{A}^{\text{line}}$, is calculated in a first instance, and the electric field is derived from it. For simplicity, we suppose that the source is located at $\phi_s = 0$. Knowing the normal polarized current source ($\mathbf{v} = \hat{\rho}$ in (1)), the vector potential can then be written as in (7) [21].

$$\mathbf{A}^{\text{line}} = \frac{\hat{x}}{4j} H_0^{(2)}\left(k_{\rho_0}\left|\rho-\rho_s\right|\right) e^{-jk_z z}, \tag{7}$$

where $\hat{x}$ is the x direction vector.

After applying the addition theorem, the vector potential has the same ϕ-dependence as the current source, as in (8).

$$\mathbf{A}^{\text{line}} = \frac{\hat{x}}{4j}\sum_{m=-\infty}^{+\infty} H_m^{(2)}\left(k_{\rho_0}\rho_s\right) J_m\left(k_{\rho_0}\rho\right) e^{j(m\phi-k_z z)}, \tag{8}$$

where the Hankel functions of the second kind has been used to represent outward-traveling waves from the line source.

By projecting the $\mathbf{A}^{\text{line}}$ along x, its ρ and ϕ components can be obtained by

$$A_\rho^{\text{line}} = \frac{1}{8j}\sum_{m=-\infty}^{+\infty} H_m^{(2)}\left(k_{\rho_0}\rho_s\right) J_m\left(k_{\rho_0}\rho\right) \times\left(e^{j\phi}+e^{-j\phi}\right) e^{j(m\phi-k_z z)}, \tag{9}$$

$$A_\phi^{\text{line}} = \frac{-1}{8}\sum_{m=-\infty}^{+\infty} H_m^{(2)}\left(k_{\rho_0}\rho_s\right) J_m\left(k_{\rho_0}\rho\right) \times\left(e^{j\phi}-e^{-j\phi}\right) e^{j(m\phi-k_z z)}. \tag{10}$$

Equations (9) and (10) can also be applied for source located in different ϕ_s by replacing ϕ with $\phi-\phi_s$. The electric and magnetic incident fields are then derived from the vector potentials in (9) and (10), which are replaced in (3) to obtain the numerical expression of the incident field from the ρ polarization component.

4.3. Scattered Field. To find the explicit boundary condition of cylinder p at order m in (5), the scattered fields from cylinders q have to be converted from local coordinate q into local coordinate p. This is solved by the Graf's addition theorem [23, 24], which is expressed as:

$$\begin{aligned} E_z^{s,q}\left(\rho_q,\phi_q\right) &= \sum_{n=-\infty}^{+\infty} B_n^q H_n^{(2)}\left(k_{\rho 0}\rho_q\right) e^{jn(\phi_q-\phi_{qs})} \\ &= \sum_{m,n=-\infty}^{+\infty} B_n^q H_{n-m}^{(2)}\left(k_{\rho 0} d_{pq}\right) J_m\left(k_{\rho 0}\rho_p\right)\Phi_{mp}^{nq} \\ &\quad\times e^{jm(\phi_p-\phi_{ps})}, \end{aligned} \tag{11}$$

where $\Phi_{mp}^{nq} = e^{jm(\phi_{ps}-\phi_{pq})} e^{jn(\phi_{pq}-\phi_{qs})}$, and (d_{pq},ϕ_{pq}) is the position of local origin O_p in local coordinate q.

Applying (11) also to $H_{m,z}^{s,q}(\rho_q,\phi_q)$, $E_{m,\phi}^{s,q}(\rho_q,\phi_q)$, and $H_{m,\phi}^{s,q}(\rho_q,\phi_q)$, together with (3), (4), and (6), the boundary condition of cylinder p at order m is finally expressed as

$$\begin{bmatrix} J_m & -H_m^{(2)} & 0 & 0 \\ \dfrac{mk_z}{k_\rho^2 r_p}J_m & -\dfrac{mk_z}{k_{\rho_0}^2\rho_p}H_m^{(2)} & \dfrac{j\omega\mu}{k_\rho}J_m' & -\dfrac{j\omega\mu_0}{k_{\rho_0}}H_m'^{(2)} \\ 0 & 0 & J_m & -H_m^{(2)} \\ -\dfrac{j\omega\epsilon}{k_\rho}J_m' & \dfrac{j\omega\epsilon_0}{k_{\rho_0}}H_m'^{(2)} & \dfrac{mk_z}{k_\rho^2\rho_p}J_m & -\dfrac{mk_z}{k_{\rho_0}^2\rho_p}H_m^{(2)} \end{bmatrix} \times \begin{bmatrix} A_m^p \\ B_m^p \\ C_m^p \\ D_m^p \end{bmatrix}$$
$$= \begin{bmatrix} E_{m,z}^{i,p}\left(r_p\right) \\ E_{m,\phi}^{i,p}\left(r_p\right) \\ H_{m,z}^{i,p}\left(r_p\right) \\ H_{m,\phi}^{i,p}\left(r_p\right) \end{bmatrix} + \sum_{q\neq p}^{P}\sum_{n=-\infty}^{+\infty}$$
$$\times \begin{bmatrix} 0 & H_{n-m}^{(2)}J_m\Phi_{mp}^{nq} & 0 & 0 \\ 0 & \dfrac{mk_z}{k_{\rho_0}^2 r_p}H_{n-m}^{(2)}J_m\Phi_{mp}^{nq} & 0 & \dfrac{j\omega\mu_0}{k_{\rho_0}}H_{n-m}^{(2)}J_m'\Phi_{mp}^{nq} \\ 0 & 0 & 0 & H_{n-m}^{(2)}J_m\Phi_{mp}^{nq} \\ 0 & -\dfrac{j\omega\epsilon_0}{k_{\rho_0}}H_{n-m}^{(2)}J_m'\Phi_{mp}^{nq} & 0 & \dfrac{mk_z}{k_{\rho_0}^2 r_p}H_{n-m}^{(2)}J_m\Phi_{mp}^{nq} \end{bmatrix}$$
$$\times \begin{bmatrix} A_n^q \\ B_n^q \\ C_n^q \\ D_n^q \end{bmatrix}, \tag{12}$$

with the following abbreviations used for clarity:

$$J_m = J_m\left(k_\rho r_p\right), \quad H_m^{(2)} = H_m^{(2)}\left(k_{\rho_0} r_p\right),$$
$$H_{n-m}^{(2)} = H_{n-m}^{(2)}\left(k_{\rho_0} d_{pq}\right). \tag{13}$$

In (12), $H_m'^{(2)}$, J_m' are the derivatives of the Hankel and Bessel functions and $E_{m,z}^{i,p}(r_p)$, $E_{m,\phi}^{i,p}(r_p)$, $H_{m,z}^{i,p}(r_p)$, and $H_{m,\phi}^{i,p}(r_p)$ are the local incident fields at order m without the phase $e^{jm(\phi_p-\phi_{ps})}$.

Equation (12) describes the scattering mechanism from multiple cylinders, and can be structured as follows:

$$\mathbf{\Lambda}_{m,p}\mathbf{\Gamma}_{m,p} = \mathbf{G}_{m,p} + \sum_{q\neq p}^{P}\sum_{n=-\infty}^{+\infty}\mathbf{F}_{mp}^{nq}\mathbf{\Gamma}_{n,q}, \tag{14}$$

$$\mathbf{\Gamma}_{m,p} = \mathbf{\Lambda}_{m,p}^{-1}\mathbf{G}_{m,p} + \sum_{q\neq p}^{P}\sum_{n=-\infty}^{+\infty}\Lambda_{m,p}^{-1}\mathbf{F}_{mp}^{nq}\mathbf{\Gamma}_{n,q}. \tag{15}$$

In (14), $\mathbf{\Lambda}_{m,p}$ corresponds to the first matrix on the left side of (12), which is the scattering matrix of cylinder p at order m. $\mathbf{\Gamma}_{m,p}$ corresponds to the scattered field parameter vector in (12). $G_{m,p}$ corresponds to the first vector on the right side of (12), which is the incident field vector to cylinder p at order m. $\mathbf{F}_{mp}^{nq}$ corresponds to the matrix on the right side of (12), which is the mutual scattering matrix of cylinder q at order n to cylinder p at order m.

Equation (15) describes two mechanisms resulting: the scattered field of cylinder p: $\mathbf{\Lambda}_{m,p}^{-1}\mathbf{G}_{m,p}$ is the first order scattered field directly from the incident field; $\sum_{q\neq p}^{P}\sum_{n=-\infty}^{+\infty}\mathbf{\Lambda}_{m,p}^{-1}\mathbf{F}_{mp}^{nq}\mathbf{\Gamma}_{n,q}$ is the higher-order scattered fields resulting from the scattered fields from the other cylinders. This mutual scattering can be understood as the process in which each cylinder is repeatedly rescattering the fields arriving at its surface. For lossy cylinders, the re-scattered fields to the outside contains less energy than the incoming fields, thus the re-scattered fields will keep decreasing as the mutual scattering repeats. This improves the convergence of the mutual scattering in the field solution towards a stable level. Consequently, the final scattered fields can be approximated by the following iterative algorithm.

(1) Let $\mathbf{\Gamma}_m^{p|(k)}$ be the updated scattered field at iteration k, $k = 0, 1, 2, \ldots$. At the initialization stage ($k = 0$), all scattered fields are 0.

(2) At iteration k, the scattered fields are updated following (15) until it reaches convergence

$$\mathbf{\Gamma}_m^{p|(k)} = \mathbf{\Lambda}_{mp}^{-1}\mathbf{G}_{mp} + \sum_{q\neq p}^{P}\sum_{n=-\infty}^{+\infty}\mathbf{\Lambda}_{mp}^{-1}\mathbf{F}_{mp}^{nq}\mathbf{\Gamma}_n^{q|(k-1)}. \tag{16}$$

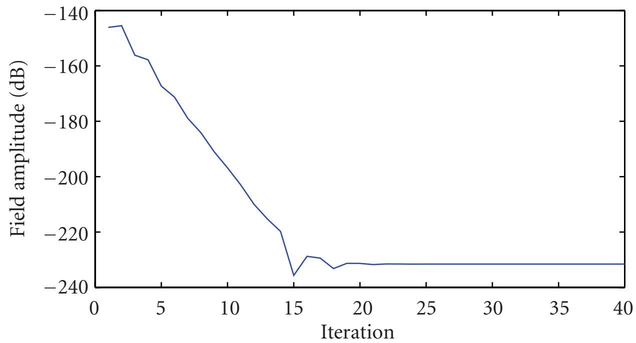

Figure 3: Convergence of the iterative approximation of line source in vertical polarization with $k_z = 0$, $I_z = 1\times10^{-10}$ A at 2.45 GHz, the source position: $\rho_s = 15$ cm, $\phi_s = 90°$, and the observation position: $\rho = 15$ cm, $\phi = 270°$.

This algorithm provides a consistent structure of the scattered fields over successive iterations expressed as

$$\mathbf{\Gamma}_m^{p|(k)} = \mathbf{\Lambda}_{mp}^{-1}\mathbf{G}_{mp} + \sum_{k=1}^{K}\mathbf{\Theta}_k,$$
$$\mathbf{\Theta}_k = \sum_1 \mathbf{\Lambda}_{mp}^{-1}\mathbf{F}_{mp}^{nq}\cdots\sum_k \mathbf{\Lambda}_{n_{k-2}q_{k-2}}^{-1}\mathbf{F}_{n_{k-2}q_{k-2}}^{n_{k-1}q_{k-1}}\mathbf{\Gamma}_n^{q|(1)}, \tag{17}$$
$$\sum_k = \sum_{n_{k-1}=-\infty}^{\infty}\ \sum_{q_{k-1}\neq q_{k-2}}^{P}.$$

The performance of the iterative algorithm is further validated by a simulation sample at 2.45 GHz, considering a vertically polarized line source with $k_z = 0$, $I_z = 1\times10^{-10}$ A, $\rho_s = 15$ cm, $\phi_s = 90°$, located on the trunk surface ($r_{\text{body}} = 14.5$ cm, $r_{\text{arm}} = 3.8$ cm, $d_{ab} = 3$ cm). The convergence of the total field amplitude in dB scale at the observation point, $\phi_s = 270°$, $\rho = 15$ cm, is provided in Figure 3. The results show a stable convergence of the field power after 15 iterations. In practice, the number of iteration is selected to be sufficiently large number ($\geq$10) that all the interested fields can converge to a stable level.

Figure 4 compares the final field solution, for both single cylinder (only trunk) and multiple cylinder scattering (with arms pending down along the sides of the trunk as in Figure 2(c)), and for a point source with tangential (z) or normal (ρ) polarizations in the azimuth plane around the trunk. The results show that for on-body channels on the trunk surface, the dominant part of the total field is determined by the incident field from the source and the scattering from the trunk, while the presence of arm scattering causes channels to fluctuate around this average value. This fluctuation varies with respect to different positions of the arms, which will generate the time-variant channel fading when in dynamic scenarios as will be discussed later. The difference between the fields for both polarizations is clear: on-body channels with tangential z-polarization have a much higher path loss around the trunk, and the arm scattering brings a larger power fluctuation. The polarization

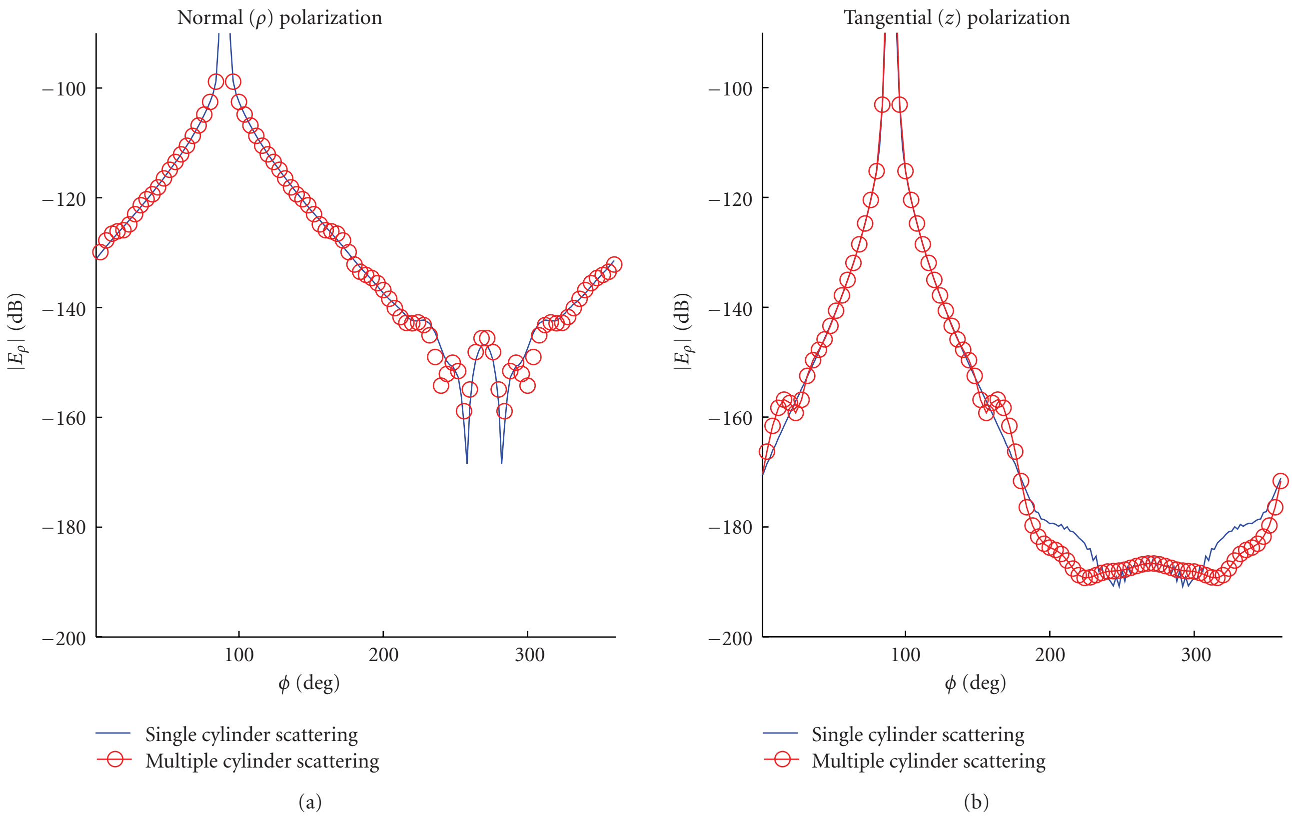

FIGURE 4: Simulation comparison of the field amplitude (dB) between single cylinder scattering and multiple cylinder scattering of a point source with $I = 10^{-10}$ A in z and ρ polarizations at 2.45 GHz around the trunk ($r_{\text{body}} = 15.4$ cm, $r_{\text{arm}} = 3.5$ cm, $d_{ab} = 3.5$ cm, $d_s = 1$ cm). The source is placed at $\rho_s = 15$ cm, $\phi_s = 90^\circ$ and the fields are computed at $\rho = 15$ cm, $\phi = [0 - 360]^\circ$.

is expected to have similar effects on the properties of the on-body channel dynamics scenarios, for example on the path loss and variance of the channel fading.

4.4. Dynamic Body Scattering Modeling. The dynamic body scattering is an extension of the above field solution obtained by incorporating the time evolution of the positions of the cylinders in the azimuth plane to simulate the arm swing during walk. In this model, we consider simple periodic trace functions $T_l(t)$ and $T_r(t)$ along the y direction to describe the left and right arm swing in Figure 2(c). The positions of the cylinders representing the arms are then expressed as

$$\begin{aligned} [x_l(t), y_l(t)] &= \left[-\left(r_{\text{arm}} + r_{\text{body}} + d_{ab}\right), T_l(t)\right], \\ [x_r(t), y_r(t)] &= \left[\left(r_{\text{arm}} + r_{\text{body}} + d_{ab}\right), T_r(t)\right], \end{aligned} \tag{18}$$

where $[x_l, y_l]$ and $[x_r, y_r]$ are the left and right arm central.

In our work, $T_l(t)$ and $T_r(t)$ are sampled by tracing a marker attached on the swinging arms of a male volunteer as in Figure 5(a). A digital camera recorded the arm swing at 30 frames per second. The averaged arm trace over one cycle is normalized into 1 s. The amplitude and the time variation of the trace functions determines most of the time-variant properties of the channel fading like the variance and deterministic waveform, hence they should be carefully selected. The considered trace functions in the simulations are shown in Figure 5(b). Usually, the synthesized time-variant fields have to be synchronized with realistic measurement observations so the field variation, that is, the local peaks of the fields along the time are matched with corresponding local peaks in measurement observations.

5. Model Validation

Our model was validated by measurements that were conducted in anechoic environment at 2.45 GHz, that is, one of the standard ISM bands for WBANs. Three small-sized antennas were fixed on the trunk surface of a male volunteer, with antenna 1 as the Tx and antennas 2 and 3 as the Rx. Two on-body channels are then formed, noted as S_{21} and S_{31}. The volunteer kept a standing posture throughout the measurements and only swung the arms to mimic the arm movements during walk. We used vector network analyzers (VNAs) to measure the transmission S-parameters of the antennas as the channel measurements. A single measurement campaign given specific locations and polarizations of the antennas lasted for 10 s. The details of the measurements are provided in Table 1.

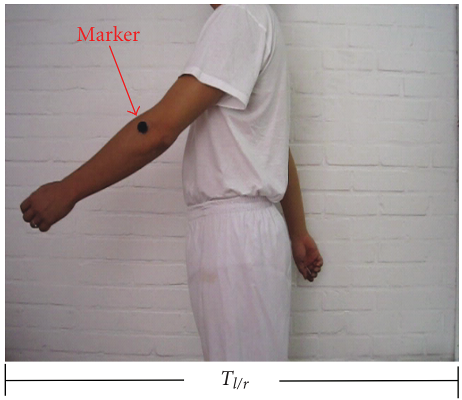

(a) Arm swing recording scenario by tracing a black marker on the arms

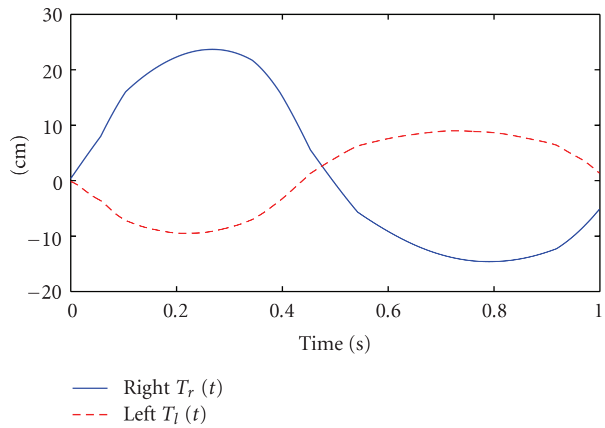

(b) The normalized trace functions over one cycle

Figure 5: The arm swing modeling.

Table 1: Measurement setup.

External environment:	anechoic
Number of antennas:	3
Measurement length:	10 s
Sampling rate:	1 ms
Human body:	male, 183 cm/78 kg
	$r_{\text{body}} = 14.2$ cm, $r_{\text{arm}} = 4.5$ cm, d_{ab}=3 cm
Body dynamics:	standing & arm swinging
Propagation range:	front side of the trunk
Polarization:	vertical & normal to the trunk surface

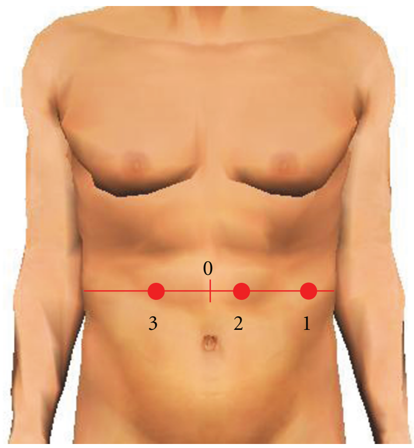

Figure 6: Tangential z-polarization scenarios. 1, 2, 3 designate the antenna allocations and 0 is the trunk center point.

We extracted the statistics of the measured on-body channels based on each measurement campaign (10 s), which are further related with their geometric description.

The simulations of the model reproduced the measurement scenarios. The simulated channels are calculated by normalizing the field solution as

$$S_{xy} = \frac{E_x}{E_y}, \tag{19}$$

where E_x is the E-field at the Rx and E_y is the E-field at a position quite close to the source. Both the deterministic time variation and the statistics of the on-body channels will be compared between the measurements and the corresponding simulations to evaluate the their similarities in different scenarios.

5.1. Tangential z-Polarization Scenarios. In the tangential z-polarization scenarios, three patch antennas (Skycross SMT-3TO10M) with z-polarization were placed around the trunk as in Figure 5.1. The antennas were placed 0.5 cm away from the trunk surface in order to mitigate the body coupling effect to the antenna efficiency. Each channel is geometrically characterized by means of the Tx position relative to the trunk center, noted as d_{10}, and the Tx-Rx propagation distances measured on the trunk surface, denoted as d_{12} and d_{13}. Propagation takes place in the azimuth (i.e., horizontal) plane from the left to the right sides of the trunk, as depicted in Figure 5.1.

The temporal fading behavior is illustrated in Figure 7, where a measurement sample of channel S_{21} with $d_{10} = 19$ cm and $d_{12} = 14$ cm is compared with the corresponding simulation. The simulation successfully matches the local peaks of the fading amplitude over the cycle and maintains a small mean squared error (MSE) of 1.21 dB with respect to the measurement. Both measurement and simulation show a symmetric waveform in the first and in the second half period, which is consistent with the regular arm swing. However, the simulated results usually display a larger dynamic variance. A possible explanation is that, given the cylindrical shape of the modeled trunk, simulations underestimate the invariant part of the channel given by the combination of the incident field and the trunk scattering, which implies that the dynamic part of the channel resulting from arm scattering is relatively increased in dB scale.

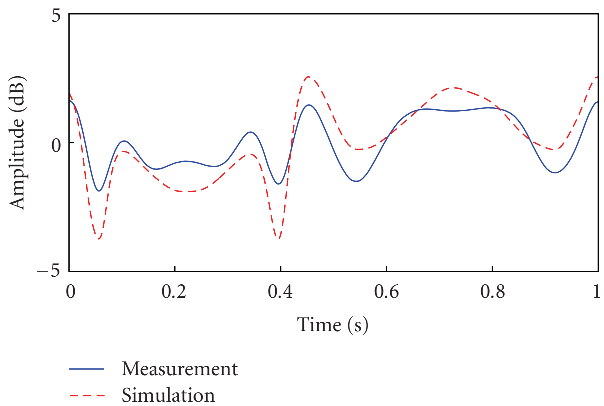

Figure 7: Waveform comparison of the normalized channel fading amplitude (dB) over one period with one measurement of S_{12} (d_{10} = 19 cm, d_{12} = 19 cm).

On-body fading statistics extracted from simulations and measurements are compared in Figures 8(a) and 8(b), respectively, for the mean, μ, and the standard deviation (std), σ of the fading amplitude in dB scale. At a specific propagation distance, the experimental spread is caused by different values d_{10}. For clarity, we only plot the average of the simulated values at each investigated propagation distance. In Figure 8(a), the simulated mean μ successfully fits the measurements, showing that the path loss around the trunk in tangential z-polarization is about 1.68 dB/cm. In Figure 8(b), the simulation results also reproduce the increasing trend of σ observed in the measurements up to 15 cm. When the propagation distance is above 15 cm, the larger simulated value of σ can again be explained by the weakening effect of the simulated invariant channel around the trunk.

The channel correlation between S_{21} and S_{31} is investigated by computing the correlation coefficient of their amplitudes in dB scale, defined as:

$$\rho_{21,31} = \frac{E\left(\left(|S_{21}|_{\mathrm{dB}} - \mu_{|S_{21}|_{\mathrm{dB}}}\right)\left(|S_{31}|_{\mathrm{dB}} - \mu_{|S_{31}|_{\mathrm{dB}}}\right)\right)}{\sigma_{|S_{21}|_{\mathrm{dB}}}\sigma_{|S_{31}|_{\mathrm{dB}}}}. \tag{20}$$

According to Figure 5.1, $\rho_{21,31}$ is related to the distance between antennas 2 and 3, d_{23}, that is the distance difference that causes the decorrelation of the two channels. In Figure 9, $\rho_{21,31}$ of two series of measurements with d_{12} = 12 and d_{12} = 14 cm are compared with the simulations, respectively. The simulation results predict a close decreasing trend of the average $\rho_{21,31}$ as a function of d_{23}, as experimentally observed.

5.2. Normal Polarization Scenarios. Measurements in the normal (ρ) polarization scenarios employed three-folded dipole antennas with normal polarization to the trunk surface. As the poles of the antenna were now pointing towards the trunk surface, the distance from the antennas to the skin was increased to 1.75 cm. In the normal polarization scenarios, the model was evaluated along two dimensions as depicted in Figure 10. In Figure 10(a), the antennas are placed around the trunk to form horizontal transmissions

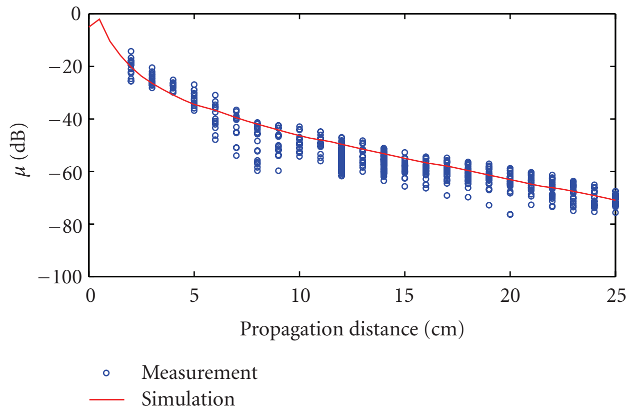

(a) μ comparison

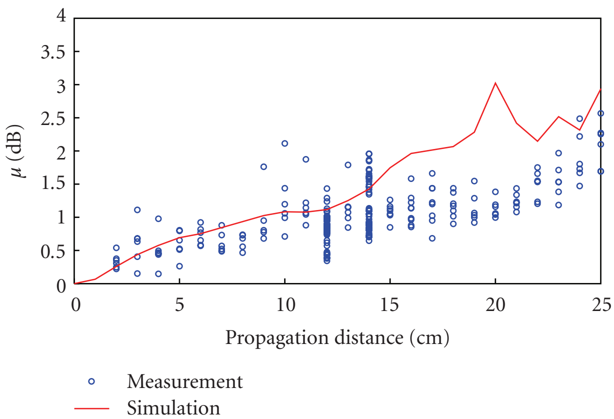

(b) σ comparison

Figure 8: Comparisons of the mean (μ) and std (σ) of the channel fading amplitude (dB) for on-body channels around the trunk in tangential z-polarization.

from the right to the left sides of the trunk. In Figure 10(b), the antennas are placed along a vertical line on the trunk to form vertical on-body channels. The positions of these channels are still described by the distance from the antenna 1 to the trunk center (d_{10}), as noted in Figure 10(b). The propagation distances, d_{12} and d_{13}, are then measured in the vertical direction.

The measured temporal fading dynamics in normal polarization scenarios are expected to deviate from simulations mainly for two reasons: (1) the dipole antenna in normal polarization contains current distributed along the normal direction, which results in much more complicated arm scattering effects and is not well approximated by a point source at a certain ρ_s; (2) the propagation along the vertical direction will get closer to the edge of the body (towards the head), thereby violating the infinite cylinder assumption. Subsequently, the comparisons in the normal polarization scenario are focused on statistical comparisons only.

5.2.1. Horizontal Propagation. Parameters μ and σ, extracted from both measurements and simulations, are compared in Figures 11(a) and 11(b), respectively. The mean μ is well predicted by the simulations, showing an average path loss

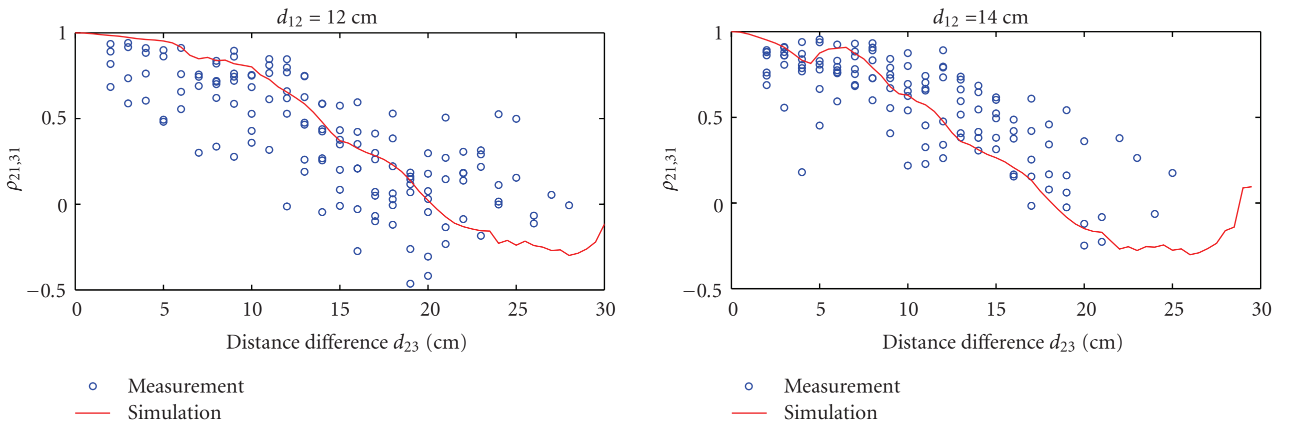

(a) d_{12} = 12 cm

(b) d_{12} = 14 cm

FIGURE 9: Comparisons of channel fading amplitude (dB) correlation coefficient $\rho_{21,31}$ for tangential z-polarization scenarios around the trunk with different lengths of d_{12}.

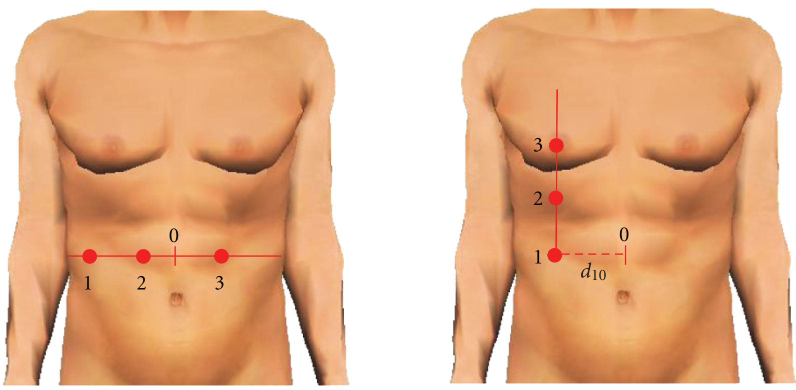

(a) Horizontal propagation

(b) Vertical propagation

FIGURE 10: Two dimensions of propagation in the normal polarization scenario.

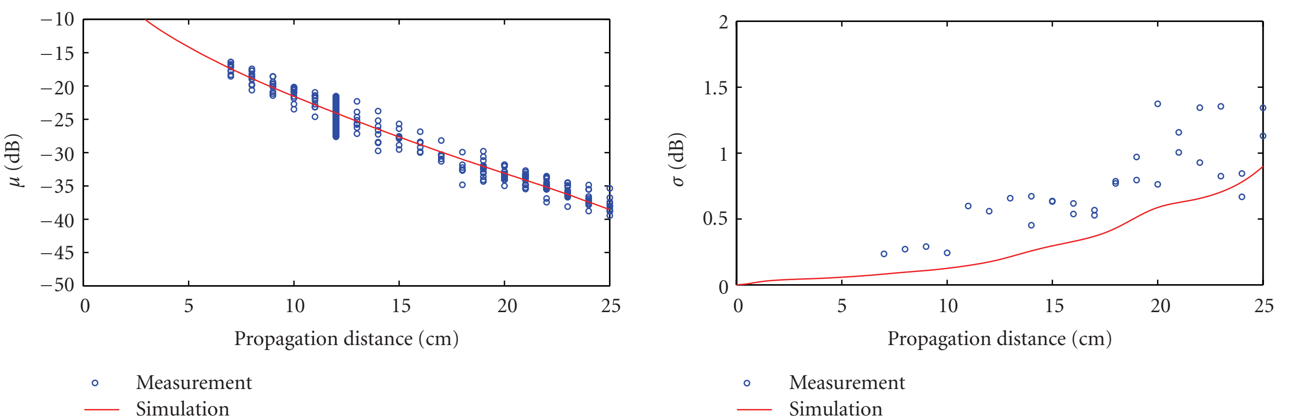

(a) μ comparisons

(b) σ comparisons in scenarios where d_{12} = 12 cm

FIGURE 11: Comparisons of the mean (μ) and std (σ) of the channel fading amplitude (dB) for on-body channels around the trunk (horizontal direction) with normal polarization.

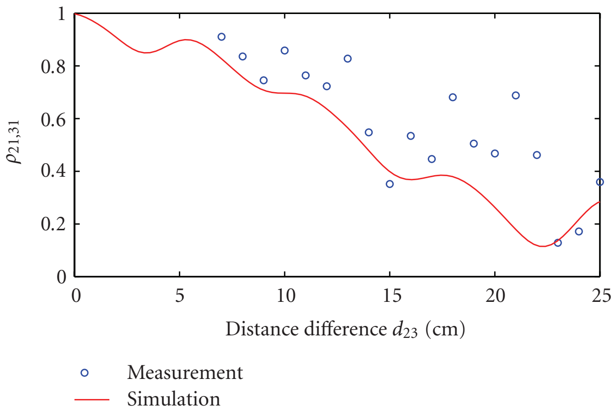

FIGURE 12: Comparison of the channel fading amplitude (dB) correlation coefficient, $\rho_{21,31}$ for normal polarization scenarios around the trunk with $d_{10} = 12$ cm and $d_{12} = 7$ cm.

of 1.1 dB/cm around the trunk in normal polarization. The comparison on σ in Figure 8(b) is based on a series of measurements with $d_{12} = 12$ cm and the corresponding simulations. Again, σ increases with the distance in both simulated and measured results. The difference between Figures 8 and Figure 11 highlights the impact of different polarizations on the fading statistics.

The channel correlation coefficient $\rho_{21,31}$, as defined by (20), is plotted in Figure 12 for a series of measurements with $d_{10} = 12$ cm, $d_{12} = 7$ cm, and for the corresponding simulations. The comparison shows a consistent decreasing trend of $\rho_{21,31}$ against d_{23}. The results of Figures 9 and 12 illustrate that, for on-body propagation around the trunk in both tangential z- and normal polarizations, the distance difference d_{23} of the overlapped channels S_{21} and S_{31} is the main decorrelation parameter.

5.2.2. Vertical Propagation. Figures 13(a) and 13(b), respectively, compare simulated and measured values of μ and σ. The simulation again provides a good prediction of μ, with an average path loss of 0.6 dB/cm for vertical on-body channels in normal polarization. These results also validate that the path loss of the propagation along the trunk is much lower than the path loss of the propagation around the trunk in normal polarization scenarios. Such difference is the result of a much stronger LOS condition for on-body channels propagating along the trunk. Consequently, it also increases the invariant part of the on-body channel, thereby yielding a smaller variance than in horizontal transmissions. In the measurements, the rotation of the arms during the arm swing causes a larger scattering effect to the vertical channels than the perfectly parallel arms assumed in the model. This explains the overall higher level of measured σ above 20 cm in Figure 13(b). Yet, the agreement is better below 20 cm.

The comparison of the channel correlation is not made since the measured range along the vertical direction is too limited to obtain relevant results.

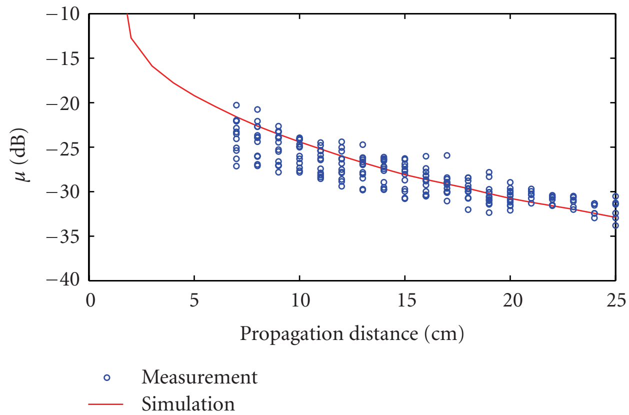

(a) μ comparison

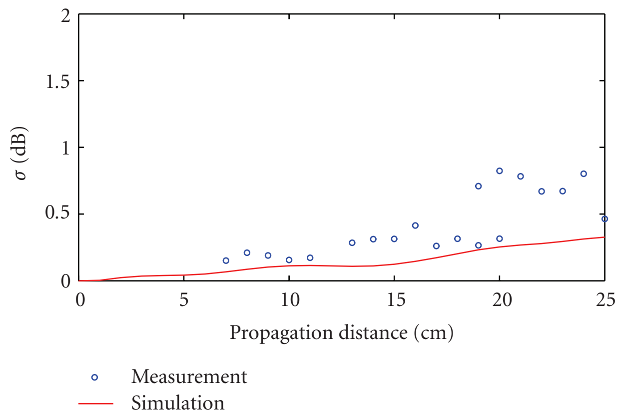

(b) σ comparison with $d_{10} = 12$ cm

FIGURE 13: Comparisons of the mean (μ) and std (σ) of the channel fading amplitude (dB) for on-body channels along the trunk (vertical direction) in normal polarization.

6. Conclusions

In this paper, we developed an analytical model of on-body transmissions on the trunk of a walking human. We investigated the impact of the antenna locations and polarizations, as well as of the body posture and motion. The dynamic scattering from the arms was analyzed with a simple description of the arm movements. A general full-wave solution of the multiple cylinder scattering by a polarized point source was derived and extended by considering time evolution. By comparisons with different measurements at 2.45 GHz, it was shown that the model successfully predicts both deterministic and stochastic aspects of the dynamic fading behavior for tangentially polarized antennas. For normally polarized antennas, only a statistical comparison was carried out, and successfully validated the model for horizontal (around the trunk) and vertical (along the trunk) transmissions. In the latter, however, the application of the model is limited to ranges below 20 cm, owing to the infinite cylinder assumption.

Our results further highlight the importance of a proper description of the arm motion, and the significant impact of the antenna polarization. The performance of our model is restricted by the infinite cylinder approximation, and the small scale of the arm swinging, so that the parallel motion assumption in the azimuth plane holds true. Furthermore, the antennas should be small enough to be well approximated by a point source. Note that the model was also validated at other frequencies in [4, 5].

Acknowledgments

This work was financed by the Région Wallone in the framework of research contract 616449 *WALIBI* within the WIST-2 program. This work was also carried out in the framework of the COST 2100 Action. The authors would also like to thank Dr. Stéphane Van Roy from the OPERA, Université Libre de Bruxelles (ULB), Belgium, and the WELCOME facility of Université catholique de Louvain (UCL), Belgium for their technical support.

References

[1] M. Patel and J. Wang, "Applications, challenges, and prospective in emerging body area networking technologies," *IEEE Wireless Communications*, vol. 17, no. 1, pp. 80–88, 2010.

[2] E. Montón, J. F. Hernandez, J. M. Blasco et al., "Body area network for wireless patient monitoring," *IET Communications*, vol. 2, no. 2, pp. 215–222, 2008.

[3] S. C. Ergen, "ZigBee/IEEE 802.15.4 summary," Tech. Rep., Advanced Technology Lab of National Semiconductor, 2004.

[4] L. Liu, S. Van Roy, P. De Doncker, and C. Oestges, "Azimuth radiation pattern characterization of omnidirectional antennas near a human body," in *Proceedings of the International Conference on Electromagnetics in Advanced Applications (ICEAA '09)*, pp. 461–464, September 2009.

[5] S. Van Roy, L. Liu, C. Oestges, and P. De Doncker, "An ultrawideband sage algorithm for body area networks," in *Proceedings of the International Conference on Electromagnetics in Advanced Applications (ICEAA '09)*, pp. 584–587, September 2009.

[6] K. Y. Yazdandoost and K. Hamaguchi, "Antenna polarization mismatch in body area network communications," in *Proceedings of the 4th European Conference on Antennas and Propagation (EuCAP '10)*, pp. 1–4, 2010.

[7] A. Fort, C. Desset, J. Ryckaert, P. De Doncker, L. Van Biesen, and S. Donnay, "Ultra wide-band body area channel model," in *Proceedings of the IEEE International Conference on Communications (ICC '05)*, pp. 2840–2844, May 2005.

[8] A. Molisch, D. Cassioli, C.-C. Chong et al., "A comprehensive standardized model for ultrawideband propagation channels," *IEEE Transactions on Antennas and Propagation*, vol. 54, no. 11, pp. 3151–3166, 2006.

[9] Y. Hao, A. Alomainy, Y. Zhao et al., "Statistical and deterministic modelling of radio propagation channels in WBAN at 2.45 GHz," in *Proceedings of the IEEE Antennas and Propagation Society International Symposium (APS '06)*, pp. 2169–2172, July 2006.

[10] L. Liu, P. De Doncker, and C. Oestges, "Fading correlation measurement and modeling on the front side of a human body," in *Proceedings of the 3rd European Conference on Antennas and Propagation (EuCAP '09)*, pp. 969–973, March 2009.

[11] E. Reusens, W. Joseph, G. Vermeeren et al., "Path loss models for wireless communication channel along arm and Torso: Measurements and simulations," in *Proceedings of the IEEE Antennas and Propagation Society International Symposium*, pp. 345–348, June 2007.

[12] Y. Zhao, A. Sani, Y. Hao, S.-L. Lee, and G.-Z. Yang, "A simulation environment for subject-specific radio channel modeling in wireless body sensor networks," in *Proceedings of the 6th International Workshop on Wearable and Implantable Body Sensor Networks (BSN '09)*, pp. 23–28, 2009.

[13] A. Fort, F. Keshmiri, G. R. Crusats, C. Craeye, and C. Oestges, "A body area propagation model derived from fundamental principles: Analytical analysis and comparison with measurements," *IEEE Transactions on Antennas and Propagation*, vol. 58, no. 2, pp. 503–514, 2010.

[14] A. Gupta and T. D. Abhayapala, "Body Area Networks: radio channel modelling and propagation characteristics," in *Proceedings of the Australian Communications Theory Workshop (AusCTW '28)*, pp. 58–63, 2008.

[15] D. Ma and W. X. Zhang, "Analytic propagation model for body area network channel based on impedance boundary condition," in *Proceedings of the 3rd European Conference on Antennas and Propagation (EuCAP '09)*, pp. 974–978, March 2009.

[16] Y. Chen, J. Teo, J. Lai et al., "Cooperative communications in ultra-wideband wireless body area networks: channel modeling and system diversity analysis," *IEEE Journal on Selected Areas in Communications*, vol. 27, no. 1, pp. 5–16, 2009.

[17] P. S. Hall and Y. Hao, *Antennas and Propagation for Body-Centric Wireless Communications*, Artech House, Norwood, Mass, USA, 2006.

[18] A. Z. Elsherbeni, "Comparative study of two-dimensional multiple scattering techniques," *Radio Science*, vol. 29, no. 4, pp. 1023–1033, 1994.

[19] R. W. Scharstein, "Acoustic scattering from two parallel soft cylinders," in *Proceedings of the IEEE Southeastcon*, pp. 534–537, April 1992.

[20] W. C. Chew, *Waves and Fields in Inhomogeneous Media*, IEEE Press, New York, NY, USA, 1995.

[21] F. Keshmiri and C. Craeye, "Wave propagation from sources with arbitrary polarization next to the human body," in *Proceedings of the IEEE International Symposium on Antennas and Propagation and the USNC/URSI National Radio Science Meeting*, 2010.

[22] A. Fort, L. Liu, F. Keshmiri, P. De Doncker, C. Oestges, and C. Craeye, "Analysis of wave propagation including shadow fading correlation for BAN applications," in *Proceedings of the 2nd IET Seminar on Antennas and Propagation for Body-Centric Wireless Communications*, vol. 2009, pp. 1–28, 2009.

[23] M. Abramowitz, I. A. Stegun, and P. M. Morse, *Handbook of Mathematical Functions*, GPO, 1964.

[24] G. N. Watson,, *Theory of Bessel Functions*, Cambridge University Press, Cambridge, UK, 1922.